PCCP

PAPER

View Article Online
View Journal

Cite this: DOI: 10.1039/c5cp02719e

Observation of direct magneto-dielectric behaviour in $Lu_3Fe_5O_{12-\delta}$ above room-temperature

P. Manimuthu,[a] R. Vidya,[bcd] P. Ravindran,[ce] H. Fjellvåg[c] and C. Venkateswaran*[a]

The coupling of dielectric and magnetic order is highly nontrivial and seldom observed in rare-earth iron garnets. Careful investigations on polycrystalline $Lu_3Fe_5O_{12-\delta}$, prepared by the solid state route, establish a direct correlation between the magnetic and dielectric order parameters. A dielectric anomaly at the magnetic ordering temperature supports this correlation. The dielectric permittivity at various magnetic fields is measured using an indigenously developed connector setup. $Lu_3Fe_5O_{12-\delta}$ exhibits a magneto-dielectric coupling of ∼6% at room temperature, which is significant in the case of a single-phase magneto-dielectric material at low fields. Rietveld refinement of the X-ray diffraction pattern, bond valence sum method, Mössbauer spectroscopy, and X-ray photoelectron spectroscopy indicate two different oxidation states of Fe. Complete structural optimizations performed using the density functional theory establish a ferrimagnetic ground state and provide structural parameters in agreement with experimental values. Electronic structure analysis shows that $Lu_3Fe_5O_{12}$ exhibits insulating behavior both in ferromagnetic and ferrimagnetic configurations. The capability of $Lu_3Fe_5O_{12-\delta}$ to exhibit room temperature magneto-dielectric response is a key factor in designing and fabricating various electronic devices and sensors.

Received 11th May 2015,
Accepted 29th May 2015

DOI: 10.1039/c5cp02719e

www.rsc.org/pccp

1. Introduction

Multiferroic materials have been attracting much interest recently because of the coexistence of ferroelectric, ferromagnetic and ferroelastic orders.[1–7] The coupling between ferroelectric and ferromagnetic orders has attracted renewed interest due to the spectacular discoveries of giant magnetoelectric (ME) [inducement of electric polarization by magnetic field (H) or *vice versa*] and magneto-dielectric (MD) effects [H-induced change in dielectric permittivity] in these materials.[8–10] The MD effect has recently been introduced to classify certain magnetic materials that possess neither spontaneous polarization nor satisfy the symmetry constraints, for a linear magnetoelectric effect, but still show some kind of coupling between the dielectric properties and magnetization.[11] The MD phenomenon itself is attractive for practical applications without ME coupling. A number of device applications have been suggested based on the MD effect, including multiple state memory elements, electric field controlled ferromagnetic resonance devices, and variable transducers with either magnetically modulated piezoelectricity or electrically modulated piezomagnetism.[12] Studies on the MD effect were mainly carried out on single phase materials, which show dielectric change under an external magnetic field.[1–3,7,13] The possibility of tuning the dielectric permittivity by an external magnetic field opens up new prospects for the basic understanding of multiferroic materials and for the design of devices based on them. But the magnetic field required for producing this effect is quite high, of the order of several tesla.[1–3,7,13,14] However, for the utilization of this effect in the above-mentioned devices, materials exhibiting an MD effect at low magnetic field (<1 T) are essential. The realization of the MD effect with a small external magnetic field is highly nontrivial and such MD materials are still rare.[15–18] Rare-earth iron garnets (RIG) with their amazingly interesting properties attract significant attention at this juncture. The materials belonging to this class were found to exhibit a relatively good magneto-dielectric effect even for a low applied magnetic field. At low magnetic fields, induced MD effects have been reported with values reaching 13% at 0.5 T and 10 K in $Y_3Fe_5O_{12}$[19] and 3% for $H < 0.2$ T below 30 K in $Tb_3Fe_5O_{12}$.[17] However, most of the practical applications demand an MD effect at room temperature.

---

[a] Department of Nuclear Physics, University of Madras, Guindy Campus, Chennai-600 025, India. E-mail: cvunom@hotmail.com; Fax: +91-044-2235 3309; Tel: +91-044-2220 2803

[b] Institute of Mathematical Sciences, Taramani, Chennai-600 113, India

[c] Centre for Materials Science and Nanotechnology, Department of Chemistry, University of Oslo, Box 1033 Blindern, N-0315 Oslo, Norway

[d] Department of Medical Physics, Anna University, Chennai-600 025, India

[e] Department of Physics, Central University of Tamil Nadu, Thiruvarur-610 004, India

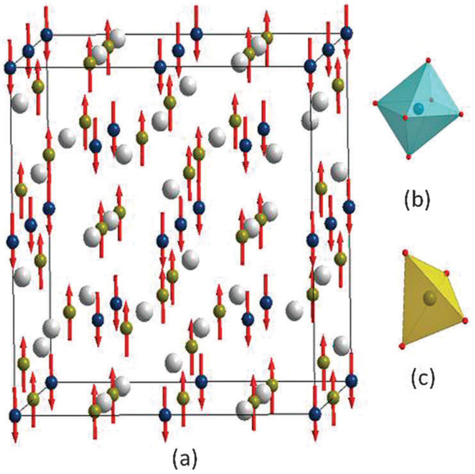

Fig. 1 (a) Magnetic structure of $Lu_3Fe_5O_{12}$. View of (b) octahedra and (c) tetrahedra.

$Lu_3Fe_5O_{12}$ is one such compound which exhibits low field MD response at room temperature.[20] $Lu_3Fe_5O_{12}$, which belongs to the RIG family, has cubic symmetry with the space group $Ia\bar{3}d$. The unit cell of $Lu_3Fe_5O_{12}$ is composed of lutetium–oxygen and iron–oxygen clusters forming three dodecahedral (LuO_8), three tetrahedral (FeO_4) and two octahedral (FeO_6) sites. The Fe^{3+} ions occupy the 16a Wyckoff position in the octahedral (0 0 0) site and the 24d Wyckoff position in the tetrahedral (0.375 0 0.25) site. The Fe^{3+} ions in the octahedral and tetrahedral sites are denoted as $Fe1^o$ and $Fe2^t$, respectively. The Lu ions are distributed over the 24c (0.125 0 0.25) Wyckoff position in the dodecahedral site and O is in the (−0.0255 0.0592 0.1514) 96h site. Fe ions in the tetrahedral and octahedral sites contribute to the magnetic properties which are coupled antiparallel with each other (Fig. 1). The Lu in the dodecahedral site does not possess magnetic moment due to the absence of unpaired electrons as Lu has $4f^{14}$ configuration. In general, the material is recognized and evidenced as a single phase MD material and therefore should have a dielectric anomaly at the magnetic ordering temperature (irrespective of the type of magnetic ordering).[16,21–23] As of now, there is no experimental evidence showing the direct coupling between magnetic and dielectric properties of $Lu_3Fe_5O_{12}$. But such a behaviour is possible in $Lu_3Fe_5O_{12}$ which has a significant range of non-stoichiometry compared to other RIGs.[20,24,25] The non-stoichiometry is accommodated in $Lu_3Fe_5O_{12}$ by the formation of oxygen vacancies. The formal oxidation state of Fe ions in $Lu_3Fe_5O_{12}$ is 3+ but during the high temperature process the oxidation state changes to 2+ owing to the loss in oxygen content.[19,20,26,27] It is well known that the varying oxidation state of transition metal ions greatly affects the physical properties.[19,20,26–29] Hence, this material is of particular interest, as both the dielectric and magnetic order parameters have a common origin *i.e.*, Fe ions facilitating good coupling in $Lu_3Fe_5O_{12}$. This paper reports the magnetic, dielectric, and MD properties of polycrystalline $Lu_3Fe_5O_{12}$ and explores the possible presence of Fe in mixed valence states, based on the observed results.

2. Materials and method of synthesis

$Lu_3Fe_5O_{12}$ ceramics were prepared employing a standard, solid-state reaction method. Raw Lu_2O_3 (99.9%) and Fe_2O_3 (99.95%) powders, weighed in stoichiometric proportions, were directly mixed together using an agate mortar and pestle for 5 hours. The resulting powder was calcined at 1173 K for 2 hours in air. The standard free energy formation temperature for $Lu_3Fe_5O_{12}$ compound is reported to be 1473 K.[24] Hence, $Lu_3Fe_5O_{12}$ ceramics were obtained by sintering at 1473 K for 5 hours in air. High temperature sintering is a diffusion controlled process by which bonding of particles in a mass of powder in the solid state occurs by atomic or molecular attraction through the application of heat. The densification is due to the decrease in the surface area and therefore a reduction in the free energy of the system during sintering occurred. High temperature sintering creates low oxygen pressure inside the furnace under normal atmospheric conditions. The Lu–Fe–O system belongs to the D-type of lanthanoid–Fe–O compound. The phase diagram of Lu–Fe–O shows four stable phases: $LuFe_2O_4$ (spinel), $LuFeO_3$ (perovskite), $Lu_2Fe_3O_7$ and $Lu_3Fe_5O_{12}$ (garnet) at elevated temperatures under controlled oxygen partial pressures.[30] Lu–Fe–O compounds are very sensitive to the atmosphere as reported elsewhere.[20,24] Due to the low oxygen pressure generated by high-temperature sintering, oxygen vacancies are formed in the $Lu_3Fe_5O_{12}$ lattice.

3. Experimental techniques

The purity and crystallinity of the sintered sample were confirmed from the X-ray diffractometer measurements (Bruker D2 PHASER) using Cu-Kα radiation and the pattern was refined according to the Rietveld method using the General Structure Analysis System (GSAS) program.[31,32] The bond valence sum method has been used to determine the oxidation state of Fe ions, based on crystallographically determined Fe–O bond distances. The oxidation state and site occupancy of Fe ions were identified through Mössbauer spectroscopy (Nucleonix, India). Field dependent (Lakeshore VSM 7410) and temperature dependent (EG & G PARC 4500) magnetic properties were determined using a vibrating sample magnetometer (VSM). The combination states of Fe 2p electrons were analyzed through X-ray photoelectron spectroscopy (XPS) (Omicron Nanotechnology, Germany). The dielectric properties were measured as a function of temperature (353 K to 723 K) using an impedance analyzer (Solatron SI 1260 impedance/gain phase analyzer) in the frequency range of 1 kHz to 1 MHz. The magneto-dielectric measurements were done with the help of an indigenously designed connector setup.[33] The salient feature of this setup is that, it is incorporated with the already existing instruments like VSM and impedance analyzer used in this study.

3.1. Computational methodology

First principles DFT calculations were performed using the Vienna Ab-initio simulation package (VASP)[34] within the projector augmented wave (PAW) method[35] as implemented by Kresse and Joubert.[36] The Kohn–Sham equations[37] were solved self-consistently using an iterative matrix diagonalization method. This is based on a band-by-band preconditioned conjugate gradient method[38] with an improved Pulay mixing[39] to efficiently obtain the ground-state electronic structure. The forces on the atoms were calculated using the Hellmann–Feynman theorem and they are used to perform a conjugate gradient relaxation. Structural optimizations were continued until the forces on the atoms had converged to less than 1 meV $Å^{-1}$ and the pressure on the cell had minimized within the constraint of constant volume and the total energy convergence. We have used an energy tolerance of 10^{-6} eV for SCF calculations. The calculations were performed within periodic boundary conditions allowing the expansion of the crystal wave functions in terms of a plane-wave basis set. The generalized gradient approximation (GGA)[40] includes the effects of local gradients in the charge density for each point which generally gives better equilibrium structural parameters. In order to include strong correlation effects GGA + U calculations have been done as implemented in the VASP-PAW method using the Dudarev scheme.[41]

On this basis, we treated explicitly 3 valence electrons for Lu ($5d^16s^2$), 8 for Fe ($3d^64s^2$), and 6 for oxygen ($2s^22p^4$). Brillouin zone integrations are performed with a Gaussian broadening[42] of 0.1 eV during all structural optimizations. We have performed a series of test calculations by gradually increasing the energy cut-off from 275 eV. Though we found that the total-energy converges to an energy cut-off value of 450 eV, we used 550 eV cut-off in an effort to obtain more accurate results with an optimum usage of computational resources. These calculations are performed with a 4 × 4 × 4 Monkhorst–Pack k-point mesh. The structures were fully relaxed for all volumes considered in the present calculations using force as well as stress minimization. Experimentally established structural data were used as input for the calculations. We have carried out calculations on non-magnetic, ferromagnetic and anti-ferromagnetic configurations.

4. Results and discussion

4.1. Structural characterization

Structural characterization of the prepared sample was performed using an X-ray diffractometer. Sharp reflection peaks are observed, indicating that the sample is properly sintered to good crystallinity. The pattern has then been refined according to the Rietveld method using the GSAS program (Fig. 2). The refinement parameters such as atomic coordination factor, multiplicity factor, occupancy, B-factor, and cell parameters are listed in Table 1. The reliability factors (χ^2 = 1.98, R_p = 2.1, R_{wp} = 2.8, R_{exp} = 3.4) obtained from Rietveld refinement of the XRD pattern indicate a better fit between the experimental and calculated patterns of the cubic ($Ia\bar{3}d$) system. From the refinement, three different crystallographic Fe–O bond distances are obtained, *i.e.*, 1.828 Å corresponds to the tetrahedral site, 2.038 Å and 2.045 Å correspond to the octahedral site. In general, only two Fe–O bond lengths are obtained which means Fe ion coordinated with four oxygen atoms in the tetrahedral site with a bond distance of 1.88 Å and in the octahedral site by six oxygen atoms with a bond distance of 2.02 Å.[43–46] Therefore, the existence of another bond length in the octahedral site may be due to two different oxidation states of the Fe ion. Using the value of ionic radii of 1.38 Å and 1.4 Å of oxygen in tetrahedral and octahedral sites, we obtain ionic radii values of 0.45 Å, 0.638 Å and 0.645 Å for the Fe ion with respect to the calculated Fe–O bond distances. According to Shannon's theory,[47] the ionic radius value of 0.45 Å corresponds to Fe^{3+} in the tetrahedral site. The other two ionic radii 0.638 Å and 0.645 Å correspond to two different oxidation states of the Fe ion in the octahedral site, which is due to the formation of oxygen vacancies as reported elsewhere.[24,47] In a widely accepted view of the microscopic description of oxygen vacancy formation, some of the Fe^{3+} ions are reduced to Fe^{2+} in the octahedral site for charge neutrality in the crystal structure.[48–51] Since, the ionic radius of Fe^{2+} is slightly greater than that of the Fe^{3+} ion, two different Fe–O bond distances are found to vary accordingly, corresponding to the octahedral site. Hence in this crystal system, the tetrahedral sublattice is completely occupied by Fe^{3+} ions while the octahedral sublattice is shared by the Fe^{3+} and Fe^{2+} ions. Though the material has a significant range of non-stoichiometry due to oxygen vacancy, no major variation in cell parameters (a = b = c = 12.279(2) Å and volume = 1851.1(1) $Å^3$) are observed, indicating that the oxygen vacancies could be isolated defect centers instead of vacancy clusters.

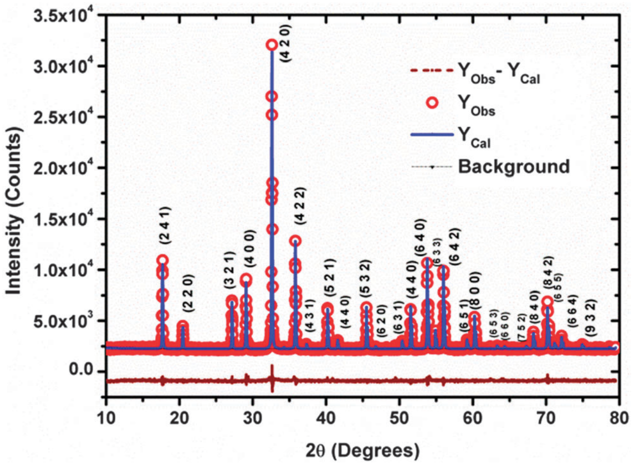

Fig. 2 Rietveld refinement of $Lu_3Fe_5O_{12-\delta}$ X-ray diffraction pattern.

4.2. Bond valence sum method

Bond length values calculated from crystallographic distances are used to predict the correct oxidation state of the Fe ion using the bond valence sum method.[52–58] Bond valences (S) are calculated according to the following equation,

$$S = \exp\left[\frac{(r_0 - r)}{B_0}\right] \qquad (1)$$

where r is the observed bond distance and r_0 and B_0 are empirically determined parameters.[52] From the Rietveld refinement of the XRD pattern, the obtained bond distance values are 2.038 Å and 2.045 Å for the octahedral site ($Fe1^o$–O1) and

Table 1 Optimized structural parameters and atom positions derived from Rietveld refinement of the XRD pattern

		Position coordinates						Cell parameter	
Atom	Oxidation state	x	y	z	Wyckoff position	B-factor	Occupancy	a (Å)	Volume (Å^3)
Lu1	Lu^{3+}	0.1250	0.0000	0.2500	24c	0.02669	1	12.279(2)	1851.1(1)
Fe1^{o}	Fe^{3+}/Fe^{2+}	0.0000	0.0000	0.0000	16a	0.03366	1		
Fe2^{t}	Fe^{3+}	0.3750	0.0000	0.2500	24d	0.02417	1		
O1	O^{2-}	−0.02743	0.0575	0.15218	96h	0.03815	1		

1.828 Å for the tetrahedral site (Fe2^{t}–O1). The two bond distances corresponding to the octahedral site are due to two different oxidation states of the Fe ion as discussed previously and therefore are classified for convenience as Fe$_1$1^{o}–O1 = 2.038 Å and Fe$_2$1^{o}–O2 = 2.045 Å. Bond valences for each Fe–O bond are calculated from the above eqn (1) using the value of r_0 = 1.759 Å for Fe^{3+}–O, r_0 = 1.734 Å for Fe^{2+}–O and B_0 = 0.37 Å.[59–61] The calculated bond valences are 2.83, 2.58, and 3.25 corresponding to Fe$_1$1^{o}, Fe$_2$1^{o}, and Fe2^{t}, which could be approximated to the known oxidation states of 3+, 2.5+, and 3.5+, respectively.

4.3. Magnetic studies

4.3.1. Mössbauer measurements. Fig. 3 shows the Mössbauer spectrum of Lu$_3$Fe$_5$O$_{12-\delta}$ at room temperature arising due to Fe in octahedral and tetrahedral sites. The dots represent the experimental data and the continuous curves represent the fitting of the experimental data. The Fe ions are magnetically ordered and are present in three different environments as evidenced from the observation of three sextets in the spectrum corresponding to tetrahedral and octahedral sites. The hyperfine magnetic fields (HF) give a clear insight into the site occupancy by providing information on which site a particular Fe ion occupies. The hyperfine magnetic fields were found to be in the order of HF (octahedral) > HF (tetrahedral).[62,63] The obtained hyperfine magnetic field values of 48 T and 51 T correspond to the octahedral site and 38 T corresponds to the tetrahedral site.[64] Based on the previous reports, the sextet of the smallest isomer shift (IS) of 0.19 mm s^{-1} with a HF of 38 T is a characteristic feature of Fe^{3+} ions in the tetrahedral site (Fe2^{t}). The other two sextets with relatively large isomer shifts *i.e.*, 0.42 mm s^{-1} and 0.45 mm s^{-1} with a HF of 51 T and 48 T correspond to Fe$_1$1^{o} and Fe$_2$1^{o}, respectively.[65,66]

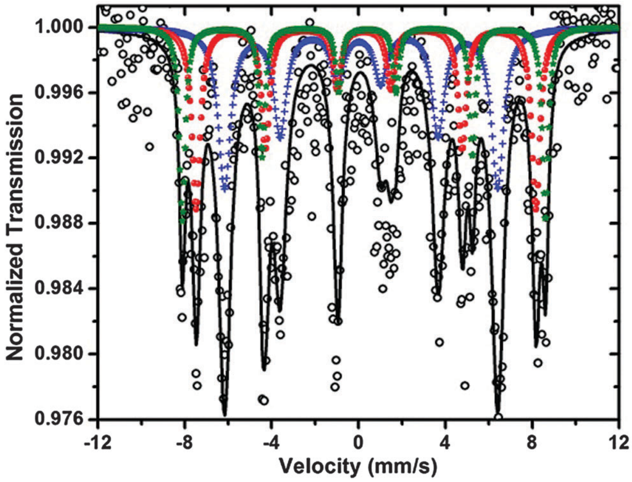

Fig. 3 Mössbauer spectrum indicating three sextets of Fe ions in the tetrahedral and octahedral sites. Open circle represents the experimental data and continuous line indicates overall fit. The symbols (.), (*), and (+) indicates Fe$_1$1^{o}, Fe$_2$1^{o}, and Fe2^{t}, respectively.

4.3.2. Vibrating sample magnetometer (VSM) measurements

(a) Field dependent magnetization (M–H) curve. Fig. 4(a) shows M–H curves of Lu$_3$Fe$_5$O$_{12-\delta}$ ceramics at 30 K and 300 K, exhibiting clear ferrimagnetic behaviour. Magnetization starts saturating at a relatively low field of ∼0.2 T with a saturation magnetization (M_S) of 23 emu g^{-1} (32.8 μ_B per unit cell) and 18 emu g^{-1} (25.6 μ_B per unit cell) at 30 K and 300 K, respectively. Also, it is found that the temperature effect on M_S is smaller than those of other garnets due to the diamagnetism of Lu^{3+}. The loop at 30 K shows a larger hysteresis compared to the loop at 300 K, which is due to the changes in the magnetic domain wall motion (or) domain rotation.[17]

(b) Temperature dependent magnetization (M–T) plot. The Curie temperature, T_C, was determined from the temperature dependent magnetization decay of the sample as depicted in Fig. 4(b). This was done by heating the sample from 303 K to 573 K in regular steps with a constant applied field of 100 Oe. From Fig. 4(b), it is seen that the orientation of the magnetic moments decreases with increasing temperature and finally vanishes around 550 K which is a characteristic feature of the material undergoing a Curie transition or phase transition. Curie transition *i.e.*, a transition from the paramagnetic to ferrimagnetic state occurs when the magnetic moment changes from zero to a non-zero value. The Kink–Point method (plotting $-\frac{\mathrm{d}M}{\mathrm{d}T}$ as a function of temperature) also shows T_C to be around 550 K (inset of Fig. 4(b)). Below T_C, the magnetic moments of Fe ions in both the tetrahedral and octahedral sites are aligned anti-parallel to each other with different magnitudes causing a resultant magnetic moment making the material to be ferrimagnetic. Above T_C, the long range magnetic ordering in the material disappears.

4.3.3. Discussion on the Mössbauer and VSM results. From the Mössbauer spectrum, it becomes difficult to accurately determine the oxidation state of Fe ions in the octahedral site whether it is Fe^{3+} or Fe^{2+}, based on the obtained isomer shift values (*i.e.*, 0.42 mm s^{-1} and 0.45 mm s^{-1}). The isomer shift value is easily influenced by parameters like temperature, pressure and other factors like the coordination number, bond length, spin state, and nature of bonding interaction with

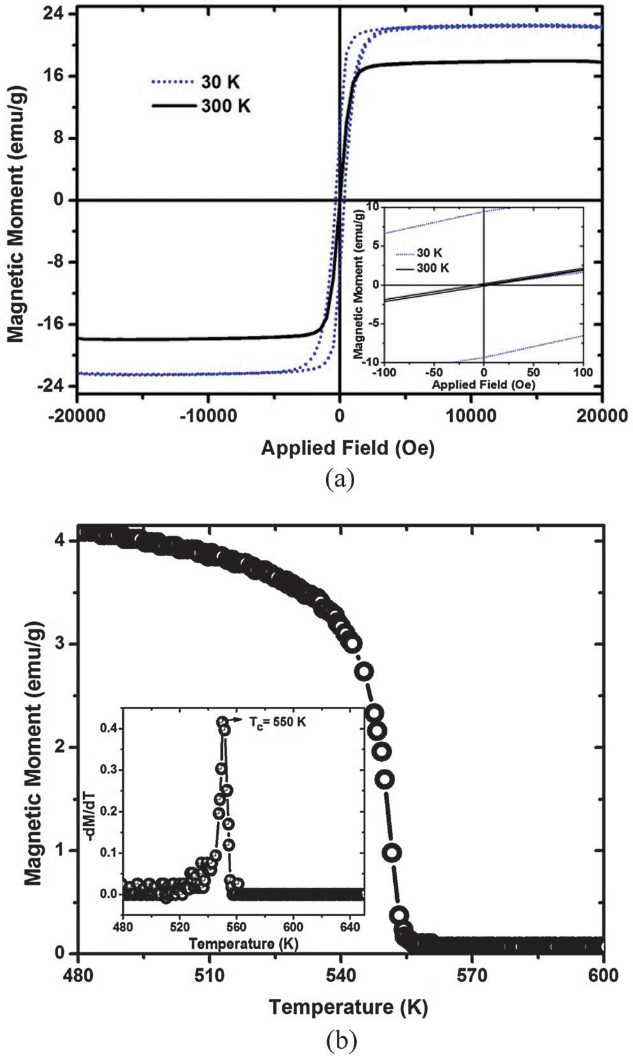

(a)

(b)

Fig. 4 (a) Magnetization *vs.* magnetic field showing clear ferrimagnetic behavior at 30 K and 300 K, inset shows the enlarged view. (b) Temperature dependent magnetization curve of $Lu_3Fe_5O_{12-\delta}$, inset shows the first derivative plot indicating paramagnetic to ferrimagnetic transition at 550 K.

neighbors, *etc.*[67] If the Fe ions were to exist only in the oxidation state of 3+, the resulting magnetic moment as per the calculations (from the relative area fraction of Fe ions in the Mössbauer spectrum) should have the value of 16 μ_B per unit cell. But M–H results clearly show the magnitude of magnetic moment to be 25.6 μ_B per unit cell. This proves the existence of two different isomer shift values corresponding to two different oxidation states of Fe ions in the octahedral site. From the Mössbauer spectrum of the two sextets, the one with the isomer shift of 0.42 mm s^{-1} with a HF of 51 T corresponds to Fe^{3+} ions (Fe_11^o) while the other one with the isomer shift of 0.45 mm s^{-1} with a HF of 48 T corresponds to Fe^{2+} ions (Fe_21^o). The loss of oxygen during sintering might have reduced some of the Fe^{3+} ions to Fe^{2+} ions giving rise to higher values for the isomer shift and smaller values for the hyperfine fields. Hence, the Fe^{2+} ions occupy the octahedral site (24%) while the Fe^{3+} ions exist both in the tetrahedral (54%) and octahedral (22%) sites. The relative area of Fe^{2+} and Fe^{3+} ions are 24% and 76%, respectively.

Considering the relative area fraction of each Fe ion in the Mössbauer spectrum, the contribution from the number of Fe ions to a unit cell is calculated. The contribution from Fe^{3+} is 21.6 (54%) at the tetrahedral site and 8.8 (22%) at the octahedral site, whereas the contribution from Fe^{2+} ions is 9.6 (24%) at the octahedral site. The general expression for one formula unit is,

$$\{Lu_3{}^{3+}\}[Fe_3{}^{3+}]^{tetra}(Fe_2{}^{3+})^{octa}O_{12}$$

Based on the above results, the formula unit can be obtained as,

$$\{Lu_3{}^{3+}\}[Fe_{2.7}{}^{3+}]^{tetra}(Fe_{1.1}{}^{3+}\cdot Fe_{1.2}{}^{2+})^{octa}O_{12-\delta}$$

The magnetic moments of Fe ions within each site are coupled parallel to each other, whereas in tetrahedral and octahedral sites the moments are antiparallel to each other. This antiparallel coupling of two unequal sites gives ferrimagnetic ordering. The direction of total magnetic moment is the same as that of moment of Fe^{3+} ions at the tetrahedral site. The derived magnetic moment as per the calculation (using Mössbauer result) for a unit cell is 25.6 μ_B per unit cell, which is in good agreement with the observed M_S value of M–H results (25.6 μ_B per unit cell). Considering the number of Fe^{2+} ions resulting from the oxygen vacancies, the calculated oxygen vacancies per formula unit is δ = 0.6 (single oxygen vacancy should create two Fe^{2+} ions) and hence the general expression of the compound in the defect state can be written as,

$$\{Lu_3{}^{3+}\}[Fe_{2.7}{}^{3+}]^{tetra}(Fe_{1.1}{}^{3+}\cdot Fe_{1.2}{}^{2+})^{octa}O_{11.4} \qquad (2)$$

4.4. X-ray photoelectron spectroscopy (XPS) study

X-ray photoelectron spectroscopy, a highly used surface-sensitive technique,[68,69] has been employed to identify the overall oxidation or chemical state of Fe ions in the prepared $Lu_3Fe_5O_{12-\delta}$ sample. The high resolution XPS peaks of Fe $2p_{3/2}$ and Fe $2p_{1/2}$ are shown in Fig. 5. The area of Fe $2p_{3/2}$ peak is greater than that of Fe $2p_{1/2}$ because of its spin–orbit (j–j) coupling; Fe $2p_{3/2}$ has degeneracy of four states whilst Fe $2p_{1/2}$ has only two.[70] In addition to that, the peaks have a broad envelope with a shoulder on the low binding energy side. The peaks have been fitted using the Gaussian–Lorentzian curve fitting method. When fitted with a single peak, the overall fit does not match with the experimental data. The best fit was obtained when each broad peak has been deconvoluted into two distinct peaks and is clearly shown in Fig. 5. This confirms the existence of Fe ions in two different oxidation states. Charge correction was carried out using the C 1s peak with a fixed value of 284.6 eV. The reported binding energies of Fe $2p_{3/2}$ and Fe $2p_{1/2}$ have been investigated by many researchers and the values are between 710.6 eV and 711.2 eV for Fe $2p_{3/2}$ and 724 eV and 724.6 eV for Fe $2p_{1/2}$.[71–73] The Fe spectrum has associated satellite peaks which are located approximately 8 eV higher than the main

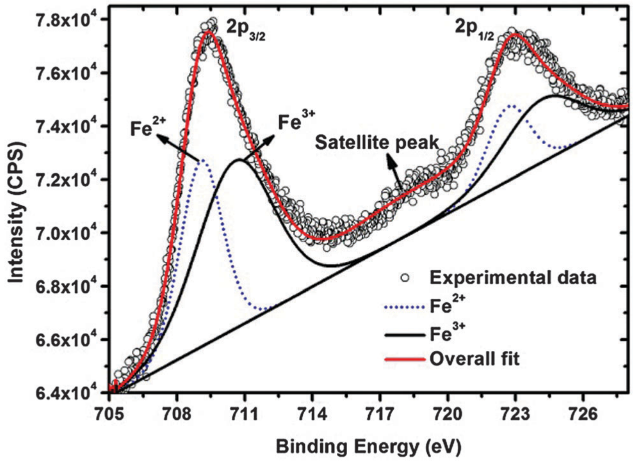

Fig. 5 High resolution X-ray photoelectron spectrum of the Fe 2p peak.

Fe $2p_{3/2}$ peak. The fitted peak positions correspond to the binding energy values of 709.1 eV and 710.8 eV for the Fe $2p_{3/2}$ peak, and 722.7 eV and 724.4 eV for the Fe $2p_{1/2}$ peak. It is well known that 709.1 eV and 722.7 eV are characteristics of Fe^{2+}, and 710.8 eV and 724.4 eV of Fe^{3+}. By evaluating the peak area, the estimated ratio of Fe^{2+} and Fe^{3+} is found to be 29% and 71%, respectively.

4.4.1. Combined XPS and VSM results. The XPS Fe $2p_{3/2}$ spectrum of the two peaks, the one with a binding energy of 710.8 eV corresponds to the Fe^{3+} ion while the other with the binding energy value of 709.1 eV corresponds to the Fe^{2+} ion. The loss of oxygen during sintering might have reduced some of the Fe^{3+} ions to Fe^{2+} ions. Considering the relative area fraction of each Fe ion in the XPS spectrum, the contribution from the number of Fe ions to a unit cell is calculated. The contribution from Fe^{3+} is 21.4 (53.5%) at the tetrahedral site and 7 (17.5%) at the octahedral site, whereas the contribution from Fe^{2+} ions is 11.6 (29%) at the octahedral site.

Based on the above results, the formula unit can be obtained as,

$$\{Lu_3{}^{3+}\}[Fe_{2.675}{}^{3+}]^{tetra}(Fe_{0.875}{}^{3+}\cdot Fe_{1.45}{}^{2+})^{octa}O_{12-\delta}$$

The derived magnetic moment as per the calculation (using XPS result) for a unit cell is 25.6 μ_B per unit cell, which is in good agreement with the observed M_S value of M–H result 18 emu g^{-1} (25.6 μ_B per unit cell). Considering the number of Fe^{2+} ions resulting from the defect, the calculated oxygen vacancies is 5.8 per unit cell (single oxygen vacancy should create two Fe^{2+} ions).

The general expression of the compound in the defect state can be written as,

$$\{Lu_3{}^{3+}\}[Fe_{2.675}{}^{3+}]^{tetra}(Fe_{0.875}{}^{3+}\cdot Fe_{1.45}{}^{2+})^{octa}O_{11.275} \quad (3)$$

4.5. Iodometric titration

The overall oxygen stoichiometry was estimated to be 11.5 ± 0.02 from the iodometric titration by the standardization of sodium thiosulfate using potassium dichromate with starch as the indicator.[74] Though there is a discrepancy in the determined oxygen content from Mössbauer (eqn (2)), XPS (eqn (3)) and iodometric titration results, the presence of off-stoichiometry is clearly evidenced from these results.

4.6. Density functional theory (DFT) calculations

We have performed complete structural optimization (including stress and force minimizations) on $Lu_3Fe_5O_{12}$ for non-magnetic, ferromagnetic, and anti-ferromagnetic configurations, by including GGA + U functionals. It may be noted that for simple GGA calculation, the system did not converge in a magnetic configuration. However inclusion of the GGA + U functional (with a U value of 6.0 eV and J = 1.0 eV) leads to significant exchange splitting, indicating that $Lu_3Fe_5O_{12}$ is a strongly-correlated oxide. The antiferromagnetic configuration is lower in energy by 3.7 eV and 5.1 eV than ferromagnetic and non-magnetic configurations, respectively. However, as determined by experimental observations, $Fe1^o$ magnetic moments are not completely cancelled by $Fe2^t$ moments, resulting in the ferrimagnetic state. The optimized lattice constant and atom positions are given in Table 2. It can be seen that the theoretically calculated lattice constant (12.390 Å) is over-estimated by 2.75% than the experimentally determined lattice constant. DFT calculations using GGA functionals normally tend to overestimate volume by ~3%. The calculated $Fe1^o$–O1 and $Fe2^t$–O1 bond lengths are 2.03 and 1.88 Å, respectively, in good agreement with the experimental values.

The magnetic moments calculated at ferromagnetic and ferrimagnetic configurations for various U values are given in Table 3. In ferromagnetic configuration, $Fe1^o$ and $Fe2^t$ sites have magnetic moments of 4.43 μ_B and 4.29 μ_B, respectively, and the total magnetic moment is 24.49 μ_B per f.u. for U = 6 eV and J = 1 eV. Owing to shorter Fe–O bond-lengths, significant covalent bonding occurs between Fe–O, leading to a finite magnetic moment of 0.2 μ_B at oxygen sites. In the ground-state antiferromagnetic configuration, magnetic moments at the octahedral Fe sublattice and the tetrahedral Fe sublattice are oppositely aligned. As there are two tetrahedral Fe atoms for

Table 2 Optimized structural parameters and atom positions derived from DFT calculation

		Position coordinates					Cell parameter	
Atom	Oxidation state	x	y	z	Wyckoff position	Occupancy	a (Å)	Volume (Å^3)
Lu1	Lu^{3+}	0.1250	0.0000	0.2500	24c	1	12.3901	1902
$Fe1^o$	Fe^{3+}	0.0000	0.0000	0.0000	16a	1		
$Fe2^t$	Fe^{3+}	0.3750	0.0000	0.2500	24d	1		
O1	O^{2-}	−0.02588	0.0548	0.15125	96h	1		

Table 3 The magnetic moments calculated at ferromagnetic and ferrimagnetic configurations for various *U* values

	Ferromagnetic configuration			Ferrimagnetic configuration		
U value (eV)	$Fe1^{o}$ (μ_B)	$Fe2^{t}$ (μ_B)	Total (μ_B per f.u.)	$Fe1^{o}$ (μ_B)	$Fe2^{t}$ (μ_B)	Total (μ_B per f.u.)
3	4.20	4.05	24.05	4.0	3.91	4.64
4	4.29	4.13	24.19	4.11	4.01	4.69
5	4.36	4.21	24.33	4.20	4.11	4.74
6	4.43	4.29	24.49	4.29	4.23	4.79

every octahedral atom, the moments are not cancelling each other resulting in a finite total magnetic moment and hence resulting in a ferrimagnetic configuration. The magnetic moments at $Fe1^{o}$ and $Fe2^{t}$ are 4.29 μ_B and 4.23 μ_B, respectively, and a total moment of 4.79 μ_B per f.u. in the ferrimagnetic state. The oxygen atoms also have a moment of 0.16 μ_B, due to covalent contribution. The magnitude of magnetic moments increases with an increase in *U* values. It may be noted that the ferrimagnetic configuration is lower in energy (by ~3 eV) than ferromagnetic configuration implying that the ferrimagnetic state is energetically more favorable, for different *U* values. As we obtained insulating ground state for a similar oxide[75] for $U = 6$ eV and $J = 1$ eV, we used the same values to study the electronic structure of $Lu_3Fe_5O_{12}$ also.

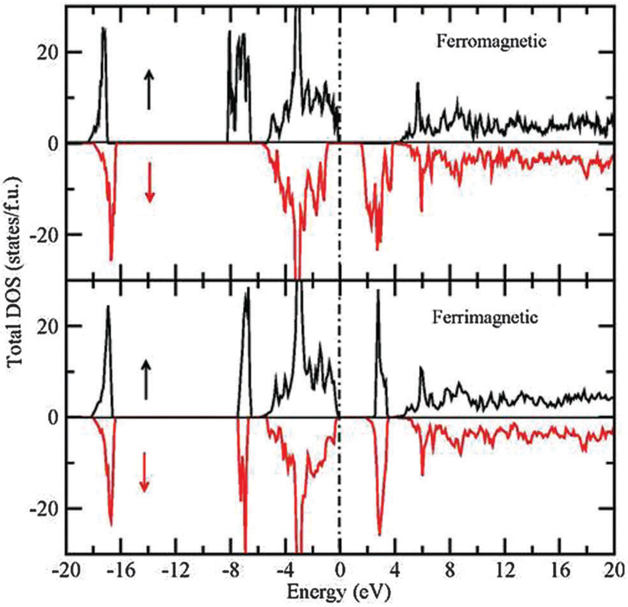

Fig. 6 Total density of states calculated using the LDA + *U* method for ferromagnetic and ferrimagnetic configurations.

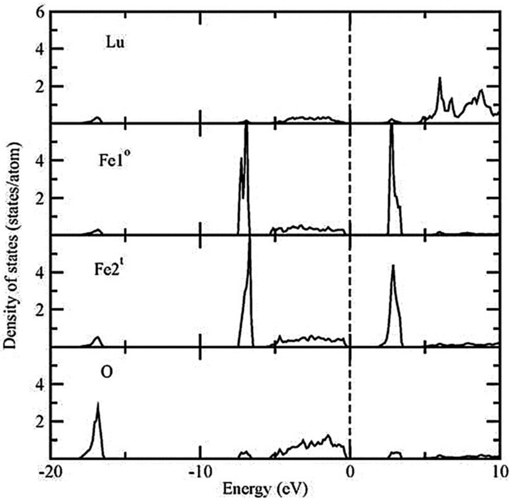

Fig. 7 Atom-specific density of states in ferrimagnetic configuration. The vertical dashed line at '0' indicates the Fermi level.

The calculated total density of states (DOS) is shown in Fig. 6 to obtain more insight on the electronic structure of $Lu_3Fe_5O_{12}$ in ferro and ferrimagnetic configurations. Interestingly, a finite energy gap of 1.39 eV can be seen between the valence band (below Fermi level; E_F) and the conduction band (above E_F) in ferromagnetic configuration. It may be noted that ferromagnetic insulators are seldom observed and receive wide attention for potential application in spintronic devices. Hence, if $Lu_3Fe_5O_{12}$ could be stabilized in ferromagnetic configuration, it would be useful for technological applications. The system remains in the insulating state in ferrimagnetic configuration as well, with an increased band gap of 1.66 eV. The atom-projected DOS in the ferrimagnetic state is shown in Fig. 7. The valence band in the top-most panel showing Lu states is almost empty, indicating that Lu has donated its valence electrons and hence forms an ionic bond with its neighbors. The Fe DOS are prominently seen between −8 and 0 eV. As O p-states are visible between −4 and 0 eV, strong covalent bonds between Fe and O can occur in this energy range. It may be noted that electronic states either participate in bonding or magnetic interaction. The presence of Fe DOS at ~−6 eV is significant and strongly localized, indicating their significant contribution to magnetic-moment of Fe atoms. As the calculated magnetic moments and DOS features are almost similar for $Fe1^{o}$ and $Fe2^{t}$, it can be inferred that both Fe atoms could be in 3+ valence states. However, it may be noted that perfectly stoichiometric composition is considered in our theoretical calculation because including oxygen vacancies will require formation of larger supercells and hence computations become intensive. On the other hand experimental samples have significant oxygen vacancies. The presence of Fe^{2+} ions can be confirmed theoretically only when oxygen vacancies are included in the calculation.

4.7. Dielectric analysis

The existence of Fe^{3+} and Fe^{2+} ions renders the material dipoles and their arrangement in the direction of applied electric field produces electric polarization. The change in dielectric permittivity (ε') *i.e.*, deciding factor of polarization as a function of temperature (353–723 K) for different frequencies (1 kHz–1 MHz) is seen in Fig. 8. The dielectric permittivity linearly increases with an increase in temperature up to 550 K, above which it starts to increase anomalously. This anomalous behavior is due to the fact that the temperature effect on Fe^{2+}

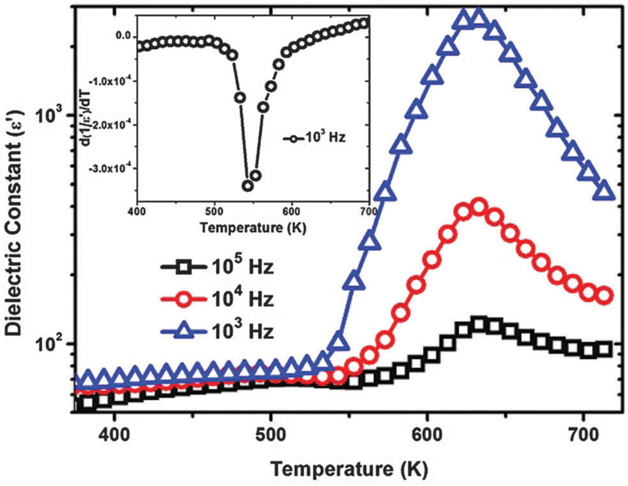

Fig. 8 Temperature dependent ε' for different frequency values shows the dielectric anomaly starts around 550 K. Inset shows the first derivative plot of $1/\varepsilon'$.

and Fe^{3+} ions produces a large shift in the electric dipole moment corresponding to polarization. The increase in ε' shows a maximum with a peak at around 625 K and then decreases with a further increase in temperature. This type of behaviour is usually seen in ferroelectric materials that undergo a phase transition from the ferroelectric to non-ferroelectric (paraelectric) phase. The aforesaid phase transition can be confirmed using the $\frac{\mathrm{d}(1/\varepsilon')}{\mathrm{d}T}$ *versus* temperature plot (inset of Fig. 8). From the plot, it is observed that there is no variation corresponding to the peak at 625 K. This clearly shows that, the peak appeared in the dielectric plot (Fig. 8) is not due to ferroelectric phase transition. The *P–E* loop recorded at room temperature with an applied field of 10 V cm^{-1} also confirms the non-ferroelectric nature of the compound (Fig. 9). Therefore, the observed behaviour is completely consistent with linear capacitor behaviour, which is the characteristic of a lossy capacitor.[76,77] Hence, the peak in the dielectric permittivity plot may be due to space charge polarization associated with oxygen vacancies.

Coming back to the dielectric plot, the dielectric anomaly starts in the vicinity of 550 K above which the magnetic ordering disappears. This is an effect of vanishing magnetic order around this temperature, which was predicted by Landau–Devonshire theory of phase transition.[78] This is ascertained from the inset of Fig. 8, where a sharp fall is clearly observed around 550 K. The possible appearance of dielectric anomalies around the magnetic ordering temperature results from the strong competition and interplay among the charge, orbital and spin degrees of freedom.[7,79,80] Therefore, the dielectric anomaly starts in the vicinity of magnetic ordering temperature due to the coupling effect of dielectric and magnetic order parameters and this also explains the intrinsic MD property of the material.

4.8. Magnetic and dielectric order coupling

To further demonstrate the coupling between magnetic and dielectric order parameters, the variation in ε' as a function of the magnetic field *i.e.*, $\frac{(\varepsilon'(H)-\varepsilon'(0))}{\varepsilon'(0)}$ is used,[81] where $\varepsilon'(H)$ and $\varepsilon'(0)$ are dielectric permittivity with the applied field H and without field, respectively. The change in ε' in the presence of magnetic field (up to 0.6 T) at various frequencies (1 kHz–1 MHz) at room temperature is shown in Fig. 10. The temperature dependent ε' shows an anomaly around its magnetic transition point, which was often taken as an evidence for MD coupling[82–84] and is clearly shown in the inset of Fig. 10. As aforementioned, Fe^{2+} and Fe^{3+} ions could produce local dipoles. When a magnetic field is applied, the spins of Fe^{2+} and Fe^{3+} ions are altered causing redistribution of charges and dipoles leading to change in polarization, resulting in the observed MD effect. Thus, the coupling between magnetic and dielectric order is evident. The change in ε' observed with

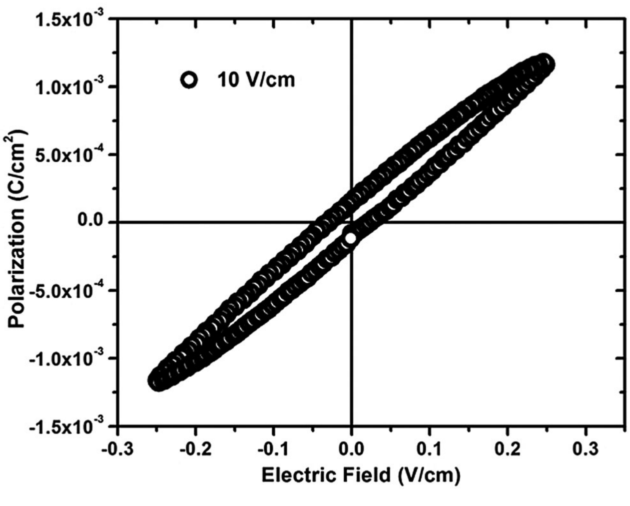

Fig. 9 Room temperature *P–E* loop showing linear capacitor behaviour.

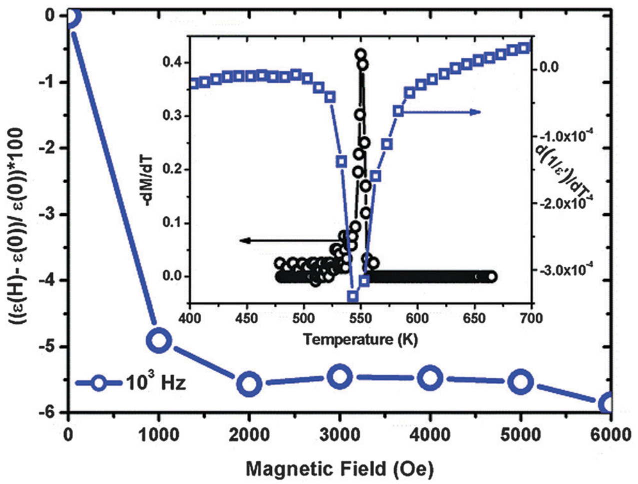

Fig. 10 Magneto-dielectric measurement showing coupling between magnetic and dielectric orders at room temperature. Inset shows clearly the anomaly of dielectric permittivity present at the magnetic ordering temperature.

a change in the applied magnetic field indicates strong coupling. The magnitude of MD coupling reaches a maximum of 6% at 10^3 Hz for 0.2 T, which is among the higher values reported for single-phase materials at room temperature and low field.

5. Conclusions

$Lu_3Fe_5O_{12-\delta}$ ceramics were prepared using the conventional solid state reaction method. Rietveld refinement of the X-ray diffraction pattern and the Mössbauer spectrum suggest the possibility of Fe ions in two different oxygen environments in octahedra. The magnetic moment calculation combined with vibrating sample magnetometer and Mössbauer results indicate the presence of oxygen vacancies and also the existence of Fe^{2+} and Fe^{3+} in the octahedral position. Moreover, the X-ray photoelectron spectrum of the Fe 2p peak clearly matches with Fe^{2+} and Fe^{3+} states. The combined results of XPS and VSM clearly support the presence of oxygen vacancies and the existence of Fe ions in the mixed valence state. The crystal structure and its parameters obtained from complete structural optimization using density functional theory-based calculations are consistent with the experimentally observed structural parameters. Furthermore, the calculations correctly reproduce the ferrimagnetic ground state upon comparing the total energies of paramagnetic, ferromagnetic, and antiferromagnetic configurations. Electronic structure analysis provides more insight into the bonding characteristics and indicates mixed iono-covalent bonding between various constituents. The calculated magnetic moments at octahedral and tetrahedral sites for ideal $Lu_3Fe_5O_{12}$ are not significantly different because the magnitude of exchange splitting in these sites is almost the same. A non-negligible magnetic moment of 0.16 μ_B at oxygen sites indicates significant covalent interaction between Fe and O atoms. However, theoretical calculations were carried out for perfectly stoichiometric composition and the oxygen vacancies present in the synthesized sample were not included in the calculations. Dielectric anomaly at the vicinity of magnetic ordering temperature indicates coupling between the magnetic and dielectric order parameters. Using an indigenously developed experimental setup, a low field magneto-dielectric response of about 6% is observed at room temperature. The considerable magneto-dielectric response of $Lu_3Fe_5O_{12-\delta}$, even for a small applied field, makes it a candidate material for application in magneto-dielectric devices.

Acknowledgements

The author Dr P. Manimuthu (PM) thanks the University of Madras for the award of University Research Fellowship (UGC-URF-2009) and Council of Scientific and Industrial Research for the award of Senior Research Fellow (CSIR-SRF-2012). Dr R. Vidya (RV) thanks Research Council of Norway for computational time at Norwegian supercomputer consortium (NOTUR). PM also thanks Dr R. Murugaraj for his help in various aspects.

References

1 T. Kimura, T. Goto, H. Shintani, K. Ishizaka, T. Arima and Y. Tokura, *Nature*, 2003, **426**, 55.
2 N. Hur, S. Park, P. A. Sharma, J. S. Ahn and S. W. Cheong, *Nature*, 2004, **429**, 392.
3 S. Weber, P. Lunkenheimer, R. Fichtl, J. Hemberger, V. Tsurkan and A. Loidl, *Phys. Rev. Lett.*, 2006, **96**, 157202.
4 N. A. Spaldin and M. Fiebig, *Science*, 2005, **309**, 391.
5 W. Eerenstein, N. D. Mathur and J. F. Scott, *Nature*, 2006, **442**, 759.
6 J. Wang, J. B. Neaton, H. Zheng, V. Nagarajan, S. B. Ogale, B. Liu, D. Viehland, V. Vaithyanathan, D. G. Schlom, U. V. Waghmare, N. A. Spaldin, K. M. Rabe, M. Wuttig and R. Ramesh, *Science*, 2003, **299**, 1719.
7 R. F. Mamin, T. Egami, Z. Marton and S. A. Migachev, *Phys. Rev. B: Condens. Matter Mater. Phys.*, 2007, **75**, 115129.
8 B. Lorenz, A. P. Litvinchuk, M. M. Gospondinov and C. W. Chu, *Phys. Rev. Lett.*, 2004, **92**, 087204.
9 H. Zheng, J. Wang, S. E. Lofland, Z. Ma, L. Mohaddes-Ardabili, T. Zhao, L. Salamanca-Riba, S. R. Shinde, S. B. Ogale, F. Bai, D. Viehland, Y. Jia, D. G. Schlom, M. Wuttig, A. Roytburd and R. Ramesh, *Science*, 2004, **303**, 661.
10 S. Dong, J. F. Li and D. Viehland, *Appl. Phys. Lett.*, 2003, **83**, 2265.
11 L. D. Landau, E. M. Lifshitz and L. P. Pitaevskii, *Electrodynamics of Continuous Media*, Pergamon, New York, 1984.
12 Q. Jiang and S. J. Gong, *Eur. Phys. J. B*, 2005, **43**, 333.
13 B. Lorenz, Y. Q. Wang, Y. Y. Sun and C. W. Chu, *Phys. Rev. B: Condens. Matter Mater. Phys.*, 2004, **70**, 212412.
14 R. P. Rairigh, G. Singh-Bhalla, S. Tongay, T. Dhakal, A. Biswas and A. F. Hebard, *Nat. Phys.*, 2007, **3**, 551.
15 T. Katsufuji and H. Takagi, *Phys. Rev. B: Condens. Matter Mater. Phys.*, 2001, **64**, 054415.
16 T. Kimura, S. Kawamoto, I. Yamada, M. Azuma, M. Takano and Y. Tokura, *Phys. Rev. B: Condens. Matter Mater. Phys.*, 2003, **67**, 180401.
17 N. Hur, S. Park, S. Guha, A. Borissov, V. Kiryukhin and S.-W. Cheong, *Appl. Phys. Lett.*, 2005, **87**, 042901.
18 T. Suzuki and T. Katsufuji, *Phys. Rev. B: Condens. Matter Mater. Phys.*, 2008, **77**, 220402 (R).
19 Y. Yamasaki, Y. Kohara and Y. Tokura, *Phys. Rev. B: Condens. Matter Mater. Phys.*, 2009, **80**, 140412.
20 X. B. Wu, X. F. Wang, Y. F. Liu, W. Cai, F. Z. Huang, X. M. Lu and J. S. Zhu, *Appl. Phys. Lett.*, 2009, **95**, 182903.
21 J. F. Scott, *Rep. Prog. Phys.*, 1979, **12**, 1055.
22 A. A. Nugroho, N. Bellido, U. Adem, G. N'enert, C. Simon, M. O. Tija, M. Mostovoy and T. T. M. Palstra, *Phys. Rev. B: Condens. Matter Mater. Phys.*, 2007, **75**, 174435.
23 H. B. Lal, R. Srivastava and K. G. Srivastava, *Phys. Rev.*, 1967, **154**, 505.
24 T. Sekine and T. Katsura, *Solid State Chem.*, 1976, **17**, 49.
25 P. Manimuthu, M. N. Jamal Ghousia Marriam, R. Murugaraj and C. Venkateswaran, *Phys. Lett. A*, 2014, **378**, 1402.
26 Y. Kohara, Y. Yamasaki, Y. Onose and Y. Tokura, *Phys. Rev. B: Condens. Matter Mater. Phys.*, 2010, **82**, 104419.

27 J. Su, X. M. Lu, C. Zhang, J. T. Zhang, S. Peng, X. B. Wu, K. L. Min, F. Z. Huang and J. S. Zhu, *J. Mater. Sci.*, 2011, **46**, 3488.

28 Y. Q. Lin and X. M. Chen, *Appl. Phys. Lett.*, 2010, **96**, 142902.

29 P. Manimuthu and C. Venkateswaran, *J. Phys. D: Appl. Phys.*, 2012, **45**, 015303.

30 M. S. Vijaya Kumar, K. Kuribayashi and K. Kitazono, *J. Mater. Res.*, 2008, **23**, 2996.

31 H. M. Rietveld, *Acta Crystallogr.*, 1967, **22**, 151.

32 A. C. Larson, R. B. Von Dreele, *General Structure Analysis System (GSAS)* (Los Alamos Laboratory Report LAUR, 1994, 86–748).

33 P. Manimuthu, H. Praveen Shanker, K. Saravana Kumar and C. Venkateswaran, *Phys. B*, 2014, **448**, 354.

34 G. Kresse and J. Hafner, *Phys. Rev. B: Condens. Matter Mater. Phys.*, 1993, **47**, R6726; G. Kresse and J. Furthmuller, *Comput. Mater. Sci.*, 1996, **6**, 15.

35 P. E. Blöchl, *Phys. Rev. B: Condens. Matter Mater. Phys.*, 1994, **50**, 17953.

36 G. Kresse and J. Joubert, *Phys. Rev. B: Condens. Matter Mater. Phys.*, 1999, **59**, 1758.

37 W. Kohn and L. J. Sham, *Phys. Rev.*, 1965, **136**, B864.

38 M. C. Payne, M. Teter, D. C. Allen, T. A. Arias and J. D. Joannopoulos, *Rev. Mod. Phys.*, 1992, **64**, 1045.

39 P. Pulay, *Chem. Phys. Lett.*, 1980, **73**, 393.

40 J. P. Perdew, in *Electronic Structure of Solids*, ed. P. Ziesche and H. Eschrig, Akademie Verlag, Berlin, 1991; J. P. Perdew, K. Burke and Y. Wang, *Phys. Rev. B: Condens. Matter Mater. Phys.*, 1996, **54**, 16533; J. P. Perdew, K. Burke and M. Ernzerhof, *Phys. Rev. Lett.*, 1996, **77**, 3865.

41 S. L. Dudarev, G. A. Botton, S. Y. Savrasov, C. J. Humphreys and A. P. Sutton, *Phys. Rev. B: Condens. Matter Mater. Phys.*, 1998, **57**, 1505.

42 C. Elsässer, M. Fähnle, C. T. Chen and K. M. Ho, *Phys. Rev. B: Condens. Matter Mater. Phys.*, 1994, **49**, 13975.

43 R. D. Shannon and C. T. Prewitt, *Acta Crystallogr., Sect. B: Struct. Crystallogr. Cryst. Chem.*, 1969, **25**, 925; R. D. Shannon and C. T. Prewitt, *Acta Crystallogr., Sect. B: Struct. Crystallogr. Cryst. Chem.*, 1970, **26**, 1046.

44 H. Pascard, *Phys. Rev. B: Condens. Matter Mater. Phys.*, 1984, **30**, 2299.

45 J. Bourgeois, M. Hervieu, M. Poienar, A. M. Abakumov, E. Elkaim, M. T. Sougrati, F. Porcher, F. Damay, J. Rouquette, G. Van Tendeloo, A. Maignan, J. Haines and C. Martin, *Phys. Rev. B: Condens. Matter Mater. Phys.*, 2012, **85**, 064102.

46 O. L. Makarova, J. Bourgeois, M. Poienar, I. Mirebeau, S. E. Kichanov, G. Andre, E. Elkaim, M. Hanfland, M. Hervieu, A. Maignan, J. Haines, J. Rouquette, C. Martin and F. Damay, *Appl. Phys. Lett.*, 2013, **103**, 082907.

47 R. D. Shannon, *Acta Crystallogr., Sect. A: Cryst. Phys., Diffr., Theor. Gen. Crystallogr.*, 1976, **32**, 751.

48 S. Geller, H. J. Williams, R. C. Sherwood and G. P. Espinosa, *J. Appl. Physiol.*, 1962, **33**, 1195.

49 B. F. Hoskins and R. L. Martin, *Aust. J. Chem.*, 1995, **48**, 709.

50 N. V. Skorodumova, S. I. Simak, B. I. Lundqvist, I. A. Abrikosov and B. Johansson, *Phys. Rev. Lett.*, 2002, **89**, 166601.

51 F. Esch, S. Fabris, L. Zhou, T. Montini, C. Africh, P. Fornasiero, G. Comelli and R. Rosei, *Science*, 2005, **309**, 752.

52 I. D. Brown and D. Altermatt, *Acta Crystallogr.*, 1985, **841**, 244.

53 H. Ichida, K. Nagai, Y. Sasaki and M. T. Pope, *J. Am. Chem. Soc.*, 1989, **111**, 586.

54 R. G. Finke, B. Rapko and T. J. R. Weakley, *Inorg. Chem.*, 1989, **28**, 1573.

55 N. Bucholz, M. LeimkUhler, L. Kiriazis and R. Mattes, *Inorg. Chem.*, 1988, **27**, 2035.

56 G. J. Palenik and S. Z. Hu, *Inorg. Chim. Acta*, 2009, **362**, 4740.

57 J. de Groot, T. Mueller, R. A. Rosenberg, D. J. Keavney, Z. Islam, J.-W. Kim and M. Angst, *Phys. Rev. Lett.*, 2012, **108**, 187601.

58 Z. Zhou, L. Guo, H. Yang, Q. Liu and F. Ye, *J. Alloys Compd.*, 2014, **583**, 21.

59 H. H. Thorp, *Inorg. Chem.*, 1992, **31**, 1585.

60 I. D. Brown, *Chem. Rev.*, 2009, **109**, 6858.

61 I. D. Brown, *The Chemical Bond in Inorganic Chemistry*, Oxford University Press, Oxford, UK, 2002.

62 N. N. Greenwood and T. C. Gibb, *Mössbauer Spectroscopy*, Chapman and Hall, London, 1971.

63 M. S. Lataifeh, S. Mahmood and M. F. Thomas, *Physica B*, 2002, **321**, 143.

64 A. Paesano Jr, S. C. Zanatta, S. N. De Medeiros, L. F. Cotica and J. B. M. Da Cunha, *Hyperfine Interact.*, 2005, **161**, 211.

65 L. Zhe, I. Shinno, Y. Danian, F. Pingqiu and Z. Yueming, *Sci. China, Ser. D: Earth Sci.*, 2001, **44**, 34.

66 G. M. Bancroft, *Mössbauer spectroscopy: An Introduction for Inorganic Chemists and Geochemists*, McGraw-Hill, London, 1973.

67 P. Ravindran, R. Vidya, H. Fjellvåg and A. Kjekshus, *Phys. Rev. B: Condens. Matter Mater. Phys.*, 2008, **77**, 134448.

68 P. Grosvenor, B. A. Kobe, M. C. Biesinger and N. S. McIntyre, *Surf. Interface Anal.*, 2004, **36**, 1564.

69 C. Suchomski, C. Reitz, C. T. Sousa, J. P. Aranjo and T. Brezesinski, *Chem. Mater.*, 2013, **25**, 2527.

70 T. Yamashita and P. Hayes, *Appl. Surf. Sci.*, 2008, **254**, 2441.

71 J. F. Moulder, W. F. Stickle, P. E. Sobol, K. D. Bomben, J. Chastain, R. C. King Jr, *Handbook of X-ray photoelectron spectroscopy*, ULVAC-PHI, Inc, Japan, 1995.

72 P. Mills and J. L. Sullivan, *J. Phys. D: Appl. Phys.*, 1983, **16**, 723.

73 D. D. Hawn and B. M. DeKoven, *Surf. Interface Anal.*, 1987, **10**, 63.

74 J. B. Basset, R. C. Denny, G. H. Jeffery and J. Mendham, *Vogels Text Book of Quantitative Inorganic Analysis*, Longman Scientific and Technical, London, UK, 1978.

75 R. Vidya, P. Ravindran, K. Knizek, A. Kjekshus and H. Fjellvåg, *Inorg. Chem.*, 2008, **47**(15), 6608.

76 J. F. Scott, *J. Phys.: Condens. Matter*, 2008, **20**, 021001.

77 J. F. Scott, *JETP Lett.*, 1989, **49**, 233.

78 L. Benguigui, *Solid State Commun.*, 1972, **11**, 825.
79 B. G. Zhong, R. W. Mu and J. H. Fang, *Solid State Commun.*, 2005, **135**, 759.
80 J. Su, X. Lu, C. Zhang, J. Zhang, H. Sun, C. Ju, Z. Wang, K. Min, F. Huang and J. Zhu, *Phys. B*, 2012, **407**, 485.
81 Y. F. Cui, Y. G. Zhao, L. B. Luo, J. J. Yang, H. Chang, M. H. Zhu, D. Xie and T. L. Ren, *Appl. Phys. Lett.*, 2010, **97**, 222904.
82 A. K. Singh, S. D. Kaushik, B. Kumar, P. K. Mishra, A. Venimadhav, V. Siruguri and S. Patnaik, *Appl. Phys. Lett.*, 2008, **92**, 132910.
83 S. Bhattacharjee, V. Panday, R. K. Kotnala and D. Panday, *Appl. Phys. Lett.*, 2009, **94**, 012906.
84 S. Chikara, O. Karneta, W. P. Crummett, L. E. DeLong, P. Schlottmann and G. Cao, *J. Appl. Phys.*, 2010, **107**, 09D910.